

**Lattice thermal transport in large-area polycrystalline graphene**

Z. Aksamija\*

*Department of Electrical and Computer Engineering, University of Massachusetts-Amherst, Amherst, Massachusetts 01003, USA*

I. Knezevic†

*Department of Electrical and Computer Engineering, University of Wisconsin-Madison, Madison, Wisconsin 53706, USA*

(Received 31 March 2014; revised manuscript received 21 June 2014; published 15 July 2014)

We study lattice thermal transport in large-area polycrystalline graphene, such as the samples grown by chemical vapor deposition (CVD) of carbon on Cu. These systems are composed of single-crystalline grains with a broad range of sizes and crystal orientations, separated by atomically rough grain boundaries. We solve the phonon Boltzmann transport equation and calculate the thermal conductivity in each grain, including scattering from the grain boundary roughness. Thermal transport in the large-area sample is considered in the Corbino-membrane geometry, with heat flowing through a network of thermal resistors and away from a pointlike heat source. The thermal transport in polycrystalline graphene is shown to be highly anisotropic, depending on the individual properties of the grains (their size and boundary roughness), as well as on grain connectivity. Strongest heat conduction occurs along large-grain filaments, while the heat flow is blocked through regions containing predominantly small grains. We discuss how thermal transport in CVD graphene can be tailored by controlling grain disorder.

DOI: [10.1103/PhysRevB.90.035419](https://doi.org/10.1103/PhysRevB.90.035419)

PACS number(s): 63.22.Rc, 65.80.Ck, 63.20.K-, 63.22.-m

**I. INTRODUCTION**

Experiments have shown that suspended graphene has high in-plane thermal conductivity—approximately  $5 \times 10^3 \text{ W m}^{-1} \text{ K}^{-1}$  at room temperature [1,2]. Theoretical calculations of the intrinsic thermal conductivity of graphene based on the relaxation-time approximation [3–5], tight binding [6], molecular dynamics (MD) [7,8], and the ballistic approximation [9] all confirmed the superior thermal properties found in experiment [10]. It was subsequently discovered that the interactions between graphene and the substrate dramatically reduce the thermal conductivity of supported samples relative to their suspended counterparts [11]. The ballistic thermal conductivity of graphene was calculated assuming coherent transmission between ideal reservoirs and reported to be isotropic in the plane of the monolayer sheet [12]; however, when graphene is cut into nanoribbons, directional anisotropy of the in-plane thermal conductivity emerges [13–15]. Moreover, disorder in the form of edge roughness has been shown to dramatically reduce the lattice thermal conductivity of nanoribbons relative to its value in large flakes [6–8,15].

Most of the aforementioned measurements relied on small graphene samples exfoliated from graphite. However, practical application of graphene require large-area samples, such as those grown by chemical vapor deposition (CVD) of carbon on a thin-film, transition-metal catalyst like Cu [16]. The CVD process can produce large-area sheets of monolayer graphene [17], opening doors to its widespread use in practical applications ranging from wafer-scale device integration to transparent electrodes for touchscreen displays. Retaining the superior transport properties of monolayer graphene, including its record-high thermal conductivity, is highly desirable for

many applications; however, CVD graphene is polycrystalline (unlike its single-crystalline exfoliated counterpart) with single-crystal grains of sizes (diameters) ranging from a few nanometers to several microns, woven together into a rich “patchwork quilt” [18].

Measurements have demonstrated that the grain size distribution in polycrystalline graphene has a roughly exponential profile, with numerous smaller, few-nanometer-sized grains clustering around fewer relatively large, micron-sized grains [19,20]. Thermal conductivity of suspended CVD graphene was found to be lower than in single-crystalline samples, with values at room temperature of approximately  $2600 \text{ W m}^{-1} \text{ K}^{-1}$  [21,22]. Still, thermal transport in polycrystalline graphene remains dominated by phonons [10,23], while the electronic contribution is negligible, similar to thermal transport in granular semiconductors [24] and in contrast to granular metals [25]. Vlasiouk *et al.* [26] measured the thermal conductivity of CVD graphene grown at different temperatures and therefore possessing varying degrees of disorder, which translates into varying characteristic domain (average grain) sizes. They found thermal conductivity to be a weak function of the domain size, with values ranging from 100 to 1000  $\text{W m}^{-1} \text{ K}^{-1}$ , depending on both the domain size and whether the data were extracted from the Raman peak shift or the Stokes/anti-Stokes ratio [26]. Faugeras *et al.* [27] similarly found the thermal conductivity of CVD graphene based on Stokes/anti-Stokes ratio in a Corbino membrane geometry to be approximately  $600 \text{ W m}^{-1} \text{ K}^{-1}$ .

Grain boundaries are expected to reduce thermal conductivity in two ways: by scattering phonons due to boundary roughness and by introducing a mode mismatch across the grain boundary (yielding the Kapitza resistance). Molecular dynamics calculations produced a boundary conductance (the inverse of the Kapitza resistance) in the range of 15 to 45  $\text{GW m}^{-2} \text{ K}^{-1}$ , significantly higher than any thermal interface conductance reported in the literature [28]. Lu and Guo [29] used the nonequilibrium Green’s function (NEGF)

\*zlatana@engin.umass.edu

†knezevic@engr.wisc.edu

technique together with the Brenner potential to study the Kapitza boundary conductance of tilted grain boundaries and found values in close agreement with the MD results ( $16.4 \text{ GW m}^{-2} \text{ K}^{-1}$  independent of the tilt angle). A direct comparison between MD and NEGF results is made difficult by the fact that NEGF calculations typically ignore anharmonic phonon interactions. Serov *et al.* [30] also used the NEGF technique for phonons to study graphene nanoribbons (GNRs) with tilt grain boundaries (GBs) and line defects (LDs). They found the transmission values for single GBs and LDs ranging from 50% to 80% of the ballistic thermal conductance. The ballistic thermal conductance per unit area of graphene,  $G_{\text{bal}} \approx 4.2 \text{ GW m}^{-2} \text{ K}^{-1}$ , can be obtained from the Landauer formula, under the assumption that graphene is placed between two thermal reservoirs with a small difference in temperature, each injecting a thermal distributions of phonons, and that, owing to the absence of scattering, each phonon manages to carry all of its energy between the injecting and collecting contacts (see, e.g., [30]). Considering that this upper bound (ballistic) thermal conductance is significantly lower than the Kapitza conductance of grain boundaries found by Bagri *et al.* [28] and Lu and Guo [29], Serov *et al.* [30] concluded that the earlier Kapitza results may have overestimated the interface conductance. Using the relaxation time approach together with a single average grain size, Serov *et al.* [30] related the transmission function from their NEGF calculations to the phonon relaxation time in order to obtain the thermal conductivity of supported polycrystalline GNR interconnects and found a strong dependence on the average grain size, with thermal conductivity ranging from 100 to 600  $\text{W m}^{-1} \text{ K}^{-1}$ , following a trend similar to the dependence of thermal conductivity in single-crystalline GNRs on their width [31,32].

However, no study to date has gone beyond single tilt GBs or LDs to address the role of structural morphology and sample-scale disorder on thermal conductivity. Sample-scale disorder is clearly seen in CVD samples in two forms: one is a random variation of grain size, shape, and crystal orientation, while the other is boundary roughness along the GBs [33]. Both forms of disorder are expected to affect thermal conductivity. Grain boundary roughness (GBR) scatters phonons, which reduces their mean-free path (mfp) from its intrinsic value in single crystalline graphene, similar to the effect of interfaces in layered three-dimensional (3D) materials like superlattices [34]; this aspect will lead to a grain-size dependence of thermal conductivity. On the other hand, grain-size variation leads to a nonuniform phonon mfp and, consequently, to local variations in the lattice thermal conductivity, analogous to 3D nanocomposites [35]. Neither of these two effects have been explored in two dimensions (2D).

In this paper we explore in-plane lattice thermal transport in large-area polycrystalline graphene. We demonstrate the sensitivity of the lattice thermal conductivity to the properties of grains and grain boundaries, in particular the grain size and boundary roughness. Rather than assuming a grain boundary scattering with a single representative grain size, we divide the 2D graphene sheet into grains of varying sizes using a Voronoi tessellation. We derive a solution to the phonon Boltzmann transport equation (pBTE) for a single grain with partially diffuse grain boundaries in the presence of competing internal scattering from umklapp phonon-phonon, isotope,

and impurity scattering processes by extending our earlier model for phonons in GNRs [31]. Based on this solution, we compute the lattice thermal conductivity in each grain of the large polycrystalline CVD graphene sheet. Based on the heat flux continuity equation for each grain, we iterate the temperature profile until a steady state is reached. Thermal transport in polycrystalline graphene samples is found to be highly anisotropic and to depend strongly on both the individual properties of the grains, i.e., their size and boundary roughness, as well as on their relative positions and grain connectivity.

This paper is organized as follows: In Sec. II we describe the 2D Voronoi tessellation used to create a polycrystalline graphene sheet in the simulation, with a grain size distribution faithful to experiment. In Sec. III we solve the pBTE for a single grain and introduce an effective GBR scattering rate (Sec. III A), derive the thermal conductivity for a single grain (Sec. III B), and describe how to obtain the steady-state temperature distribution based on the heat flux continuity equation (Sec. III C). Results are presented in Sec. IV. We conclude with a summary and some final remarks in Sec. V.

## II. 2D VORONOI TESSELLATION FOR POLYCRYSTALLINE GRAPHENE

Since CVD graphene grows from many nucleation points on the Cu thin film, we envision the growth process as the grains expanding uniformly and isotropically outward from each nucleation point until two adjacent patches of graphene begin to meet [36]. At the contact point the growth halts and a GB forms perpendicular to the line connecting the two nucleation points. Such growth can be captured using a Voronoi tessellation (VT) of the 2D space. The 3D VT has been used widely to model the structure and transport in polycrystalline and nanocomposite materials such as ZnO [37] and SiC [38], but it has not yet been applied to mathematically model the grain structure of CVD graphene. The VT is a mathematical dual to the standard and widely used Delaunay triangulation [39] (which often forms the discretization used in the popular finite-element method), and is based on exactly the same process as how we envision the growth of CVD graphene: The VT starts with a set of seed points in the 2D plane and determines a division of space into distinct, nonoverlapping polygons, following the same rules of construction of Wigner-Seitz cells [40], except on the scale of grains instead of lattice cells.

A common and efficient way of determining the VT is to start from each point and grow radially outward until two neighboring areas meet and begin to overlap [39], which mimics the CVD growth process and produces grains which visually resemble the images of CVD grown graphene (Fig. 1). Once the VT is determined, several key properties can be calculated from it, including the characteristic size of each grain (defined by the square root of its area  $S_i$ ) and the resulting distribution of grain sizes. In order to reproduce the exponential behavior of the size distribution which was observed experimentally [20], we find that the locations of the starting points in 2D space (the “nucleation” points) from which the VT is calculated has to be clustered rather than distributed uniformly at random, as the uniform random

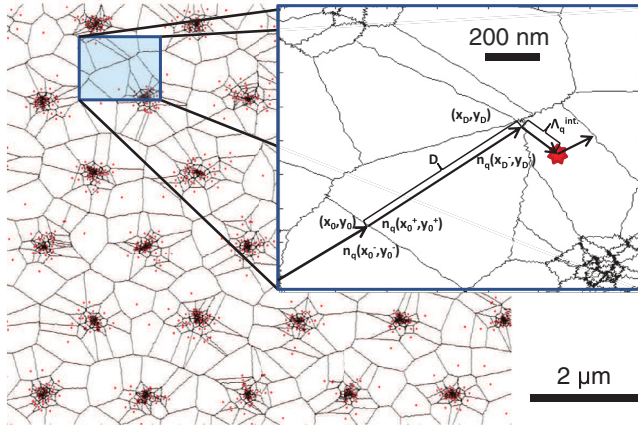


FIG. 1. (Color online) Grains in polycrystalline graphene computed based on the 2D Voronoi tessellation. Inset shows a phonon traveling through a polycrystalline sample, encountering rough grain boundaries. Grain boundaries are shown with  $\Delta = 1$  nm rms roughness.  $D$  denotes the distance a phonon mode with wave vector  $\vec{q}$  has traveled inside a particular grain.

distribution leads to a Poisson-Voronoi process [41]. As shown in Fig. 1, we group the points into clusters with 50 points each. Around the center of each cluster, points in each cluster have a normal (Gaussian) distribution of positions. We have found that distributing cluster centers uniformly at random often leads to a clustering of clusters, which results in a final distribution of grain sizes that is closer to the log-normal than the experimentally relevant exponential distribution. Therefore, we place cluster centers on a triangular lattice, with a typical center distance of  $2 \mu\text{m}$ . Such cluster center placement gives each cluster optimal room and minimizes their overlap, and results in the final grain size distributions well aligned with experiment [18,20], as depicted in Fig. 2. The resulting grains often resemble deformed and elongated rectangles due to the clustering. As shown by Bartkowiak and Mahan [37], an ordered hexagonal lattice has coordination number six (every grain has six neighbors). As disorder grows,

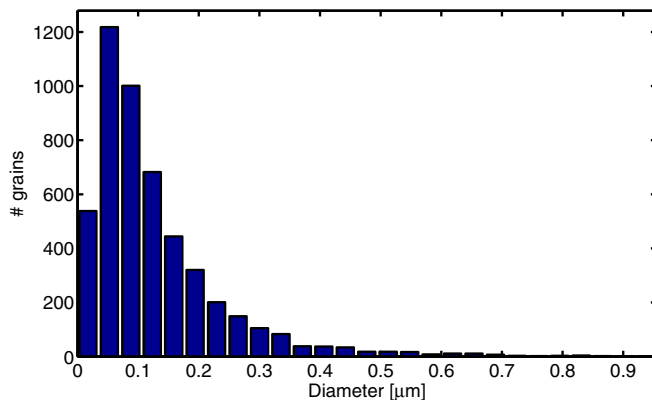


FIG. 2. (Color online) Histogram of a grain-size distribution obtained based on the Voronoi tessellation, which corresponds closely with experiment. The distribution represents a  $10 \times 10 \mu\text{m}^2$  polycrystalline graphene sheet with 5000 grains and an average grain diameter of about 120 nm.

the formation of grains with larger and smaller coordination numbers can occur, resulting in grains as few as three neighbors (having triangular shape). However, we have confirmed that the average number of neighbors remains close to six even with increased disorder due to clustering.

### III. PHONON TRANSPORT MODEL

Since the dominant carriers of heat in graphene are phonons, we focus on the lattice component of thermal conductivity and neglect the relatively small electronic contribution [10,23]. At room temperature in graphene, the dominant phonon wavelength for thermal transport purposes is about 2–3 nm, while the typical grain size (see Fig. 2) is about 120 nm. A typical phonon is much “smaller” than a typical grain, so the semiclassical transport picture is justified. Therefore, we model lattice thermal transport in each grain of the polycrystalline structure by using the linearized pBTE. Our approach to solving the pBTE is broken into several steps. The grain structure of the polycrystalline graphene, as modeled by the Voronoi tessellation, represents a natural discretization of the problem. Therefore, we will first solve the pBTE for an individual grain in order to obtain the expression for the thermal conductivity tensor for each grain. We focus here on the effects of roughness at the grain boundaries on the lattice thermal transport, as captured by the spatial variation in the phonon distribution function. In a steady state, the phonon distribution function  $N_{b,\vec{q}}(x,y)$  is a function of the phonon branch  $b$ , wave vector  $\vec{q}$ , and position in the 2D  $xy$  plane and is governed by the time-independent pBTE:

$$\vec{v}_{b,\vec{q}} \cdot \nabla N_{b,\vec{q}}(x,y) = -\frac{N_{b,\vec{q}}(x,y) - N_{b,\vec{q}}^0(T)}{\tau_{b,\vec{q}}^{\text{int}}}, \quad (1)$$

where  $\tau_{b,\vec{q}}^{\text{int}}$  is the total relaxation time due to all internal scattering mechanisms, including umklapp phonon-phonon, isotope, impurity, and, for supported graphene samples, substrate interactions. Based on our past work [15,31], we obtain  $\tau_{b,\vec{q}}^{\text{int}}$  in the usual single-mode relaxation time approximation (SM-RTA). Although the SM-RTA does not fully capture the details of all the anharmonic phonon-phonon scattering in intrinsic graphene [42], in particular the redistribution of modes due to normal phonon scattering [43], it is adequate for our purposes since our previous work has shown it to produce accurate results for finite-sized samples in the presence of edge roughness scattering in both suspended [15] and supported [31] GNRs. We note, however, that the derivation that follows is independent of how  $\tau_{b,\vec{q}}^{\text{int}}$  is calculated, whether by SM-RTA or iteratively.

Under small applied temperature gradients, the steady-state solution of the pBTE has two components: one arising from the temperature variation due to the neighboring grains having different temperatures, and a second component due to the spatial variation arising from phonon scattering at the rough grain boundaries [44]. Therefore, we write  $N_{b,\vec{q}}(x,y) = N_{b,\vec{q}}^0(T) + n_{b,\vec{q}}(x,y)$ , where  $N_{b,\vec{q}}^0(T)$  captures the effect of position-dependent temperature  $T(x,y)$ , while the second term  $n_{b,\vec{q}}(x,y)$  captures the more “explicit” position dependence originating from GBR scattering. Introducing this partition

into the time-independent pBTE (1), we obtain

$$(\vec{v}_{b,\vec{q}} \cdot \nabla T) \frac{dN_{b,\vec{q}}^0(T)}{dT} + \vec{v}_{b,\vec{q}} \cdot \nabla n_{b,\vec{q}}(x,y) = -\frac{n_{b,\vec{q}}(x,y)}{\tau_{b,\vec{q}}^{\text{int}}}. \quad (2)$$

Before introducing the grain boundaries, let us consider the homogenous case and a phonon mode  $(b,\vec{q})$  propagating from  $(x_0, y_0)$  a distance  $d$  to  $(x_d, y_d)$  in the direction of mode velocity  $\vec{v}_{b,\vec{q}}$ . In the absence of grain boundaries, the steady-state solutions at any two points along the direction of propagation have to be equal,  $n_{b,\vec{q}}(x_0, y_0) = n_{b,\vec{q}}(x_d, y_d)$ , otherwise phonons would either be accumulated [if  $n_{b,\vec{q}}(x_0, y_0) > n_{b,\vec{q}}(x_d, y_d)$ ] or depleted [if  $n_{b,\vec{q}}(x_0, y_0) < n_{b,\vec{q}}(x_d, y_d)$ ] in the region between  $(x_0, y_0)$  and  $(x_d, y_d)$ . Consequently,  $n_{b,\vec{q}}(x_0, y_0)$  has to be constant along the direction of propagation, which implies that  $\vec{v}_{b,\vec{q}} \cdot \nabla n_{b,\vec{q}}(x,y) = 0$  and the solution has the familiar homogeneous “bulk” form with no explicit position dependence:

$$n_{b,\vec{q}}^{\text{bulk}} = -\tau_{b,\vec{q}}^{\text{int}} (\vec{v}_{b,\vec{q}} \cdot \nabla T) \frac{dN_{b,\vec{q}}^0(T)}{dT}. \quad (3)$$

Once grain boundaries are introduced, the solution becomes position dependent along the direction of propagation of the phonon mode  $(b,\vec{q})$  because of two competing processes: One is scattering at the grain boundaries, which partially randomizes the direction of propagation of the incoming phonons, and the other is scattering inside the grain. If there is a grain boundary at a point  $(x_0, y_0)$ , the solution inside the grain starts from the boundary value at  $(x_0^+, y_0^+)$  and approaches the bulk value in Eq. (3) away from the boundary [31],

$$n_{b,\vec{q}}(x_d, y_d) = n_{b,\vec{q}}^{\text{bulk}} [1 - \exp(-d/\Lambda_{b,\vec{q}}^{\text{int}})] + n_{b,\vec{q}}(x_0^+, y_0^+) \exp(-d/\Lambda_{b,\vec{q}}^{\text{int}}), \quad (4)$$

for a phonon wave leaving the boundary at  $(x_0, y_0)$  and traveling a distance  $d$  in the direction of  $\vec{v}_{b,\vec{q}}$ . Inside the grain, phonons will scatter due to interactions with other phonons, isotopes, impurities, and, for supported samples, substrate interactions; these interactions are captured by the mfp due to internal scattering,  $\Lambda_{b,\vec{q}}^{\text{int}} = \nu_{b,\vec{q}} \tau_{b,\vec{q}}^{\text{int}}$ .

At the grain boundary phonons will interact with the atomic-scale roughness, which is formed at the boundary during the growth [33]. Some fraction  $p_{\vec{q}}$  of the incoming phonons will pass through unscattered, while the rest  $(1 - p_{\vec{q}})$  will be absorbed by the boundary and re-emitted in a random direction (diffuse part). The following boundary condition holds for partially coherent transmission of the phonon wave

$$N_{b,\vec{q}}(x_0^+, y_0^+) = p_{\vec{q}} N_{b,\vec{q}}(x_0^-, y_0^-) + [1 - p_{\vec{q}}] N_{b,\vec{q}}^0(T), \quad (5)$$

where  $+$  and  $-$  superscripts refer to just before and just after the grain boundary at  $(x_0, y_0)$ , respectively, and  $N_{b,\vec{q}}^0(T)$  is the equilibrium Bose-Einstein phonon distribution. Based on our previous work on phonon scattering from rough boundaries in graphene ribbons [15,31], we employ a momentum-dependent specularly parameter

$$p_{\vec{q}} = \exp(-4q^2 \Delta^2 \sin^2 \Theta_{\text{GB}}). \quad (6a)$$

As originally proposed by Graebner *et al.* [45],  $p_{\vec{q}}$  represents the fraction ( $0 \leq p_{\vec{q}} \leq 1$ ) of unscattered phonons to the total number of phonons that impinge on the rough boundary with

a given rms roughness height  $(\Delta)$ . This expression allows us to connect the specularly parameter  $p_{\vec{q}}$  directly to the rms magnitude of the GBR  $\Delta$ , the phonon wave vector  $\vec{q}$ , and the angle  $\Theta_{\text{GB}}$  between the incident phonon and the normal to the grain boundary, so that GBR scattering has the expected dependence on the phonon wavelength: Large wavelengths pass through unaffected, while small wavelengths scatter diffusely from the GBR. We assume that  $\Theta_{\text{GB}}$  is random, obeying a uniform distribution, and we average  $p_{\vec{q}}$  to obtain its effective value as

$$\bar{p}_q = \frac{1}{2\pi} \int_0^{2\pi} p_{\vec{q}} d\Theta_{\text{GB}} = e^{-2q^2 \Delta^2} I_0(2q^2 \Delta^2), \quad (6b)$$

where  $I_0$  is the modified Bessel function of the first kind.

We return now to consider the number of phonons entering the grain at  $(x_0, y_0)$  and leaving it at  $(x_D, y_D)$ , where the distance  $D$  is the distance traveled by a phonon in mode  $(b,\vec{q})$  inside that grain before reaching the next grain boundary (Fig. 1). Substituting  $N_{b,\vec{q}}(x_0, y_0) = N_{b,\vec{q}}^0(T) + n_{b,\vec{q}}(x_0, y_0)$  into Eq. (5), we find the boundary condition on the spatially varying part of the solution as  $n_{b,\vec{q}}(x_0^+, y_0^+) = p_{\vec{q}} n_{b,\vec{q}}(x_0^-, y_0^-)$ . Since the solution for mode  $(b,\vec{q})$  is not directly dependent on other modes (other than through phonon-phonon scattering, which is captured at the level of the internal mfp  $\Lambda_{b,\vec{q}}^{\text{int}}$ ), the number of phonons in mode  $(b,\vec{q})$  entering the grain at  $(x_0, y_0)$  has to equal the number leaving it at  $(x_D, y_D)$  in order for the solution to be in steady state. In other words,  $n_{b,\vec{q}}(x_0^-, y_0^-) = n_{b,\vec{q}}(x_D^-, y_D^-)$ , from which we obtain  $n_{b,\vec{q}}(x_0^+, y_0^+) = p_{b,\vec{q}} n_{b,\vec{q}}(x_D^-, y_D^-)$  by using the boundary condition at  $(x_0, y_0)$ . Introducing this expression into Eq. (4) allows us to solve for  $n_{b,\vec{q}}$  as

$$n_{b,\vec{q}}(x_D, y_D) = n_{b,\vec{q}}^{\text{bulk}} \left[ 1 - \frac{(1 - \bar{p}_q) \exp(-D/\Lambda_{b,\vec{q}}^{\text{int}})}{1 - \bar{p}_q \exp(-D/\Lambda_{b,\vec{q}}^{\text{int}})} \right]. \quad (7)$$

The solution in the presence of grain boundaries is lower than the bulk solution, which will translate into the polycrystalline graphene having lower thermal conductivity than its single-crystalline counterpart. The reduction will be grain specific, and will depend on the sizes of individual grains (through  $D$ ) and on GBR (through  $\bar{p}_q$ ).

### A. Effective GBR scattering rate

An effective scattering rate  $\Gamma_i^{\text{GBR}}$  due to the interactions of phonons with the GBR in the  $i$ th grain can be defined by averaging the solution in Eq. (7) over the grain [44,46]

$$\Gamma_{b,\vec{q}}^{\text{int}} n_{b,\vec{q}}^{\text{bulk}} = [\Gamma_{b,\vec{q}}^{\text{int}} + \Gamma_{i,b,\vec{q}}^{\text{GBR}}] \langle n_{b,\vec{q}}(x,y) \rangle. \quad (8)$$

Here  $\langle \dots \rangle$  denotes a spatial average over the grain. Combining Eqs. (3) and (8) with the pBTE from Eq. (2) we obtain for the GBR rate

$$\Gamma_{i,b,\vec{q}}^{\text{GBR}} = \langle \vec{v}_{b,\vec{q}} \cdot \nabla n_{b,\vec{q}}(x,y) \rangle / \langle n_{b,\vec{q}}(x,y) \rangle,$$

which is evaluated analytically to obtain the final expression for the effective GBR scattering rate

$$\Gamma_{i,b,\vec{q}}^{\text{GBR}} = \frac{\nu_{b,\vec{q}}}{D_i} F_{i,b,\vec{q}} / \left[ 1 - \frac{\Lambda_{b,\vec{q}}^{\text{int}}}{D_i} F_{i,b,\vec{q}} \right], \quad (9)$$

with  $D_i$  being the average distance a phonon travels inside the  $i$ th grain. Adamyan and Zavalniuk [47] showed that  $D_i$

can be related to the surface area of the grain  $S_i$ , calculated for each grain from the VT, as  $D_i = f\sqrt{S_i}$ , where  $f$  is the dimensionless form factor which captures the particularities of the specific geometry of each grain. (For grains roughly approximated as disks,  $f = \frac{8}{3\pi^{3/2}} \approx 0.48$ .) Parameter  $F_{i,b,\vec{q}}$  captures the competition between GBR scattering and internal scattering:

$$F_{i,b,\vec{q}} = \frac{(1 - \bar{p}_q)[1 - \exp(-D_i/\Lambda_{b,\vec{q}}^{\text{int}})]}{1 - \bar{p}_q \exp(-D_i/\Lambda_{b,\vec{q}}^{\text{int}})}. \quad (10)$$

The GBR scattering rate  $\Gamma_{i,b,\vec{q}}^{\text{GBR}}$  in Eq. (9) can be added to the rates due to other scattering processes internal to the grain to obtain the total scattering rate of mode  $(b,\vec{q})$  in grain  $i$  as  $\Gamma_{i,b,\vec{q}} = \Gamma_{b,\vec{q}}^{\text{int}} + \Gamma_{i,b,\vec{q}}^{\text{GBR}}$  [31].

Let us put this result in a broader context: We solved the pBTE with internal scattering mechanisms (phonon-phonon and mass difference) while we introduced rough GBs through boundary conditions on phonon mode occupations. It turns out that, from the total phonon occupation in the presence of rough GBs, we can extract a single effective grain boundary scattering rate, which captures the interplay between internal and boundary scattering [34] and is sensitive to how large a grain is with respect to the bulk mean-free path of a given mode. The effective GB scattering rate therefore differs for large and small flakes: For a mode that scatters many times between two boundaries ( $D_i/\Lambda_{b,\vec{q}}^{\text{int}} \gg 1$ ),  $\Gamma_{i,b,\vec{q}}^{\text{GBR}} = \frac{\nu_{b,\vec{q}}}{D_i}(1 - \bar{p}_q)$ , which is a well-known expression for single-boundary scattering, i.e., the phonon “forgets” about the first boundary before reaching the second. In contrast, for modes that move almost ballistically between the two GBs ( $D_i/\Lambda_{b,\vec{q}}^{\text{int}} \ll 1$ ), we obtain  $\Gamma_{i,b,\vec{q}}^{\text{GBR}} = \frac{2\nu_{b,\vec{q}}}{D_i} \frac{1 - \bar{p}_q}{1 + \bar{p}_q}$ , which is a well-known expression derived by Ziman [48]. Considering that the mean-free path due to internal scattering in single-crystalline suspended graphene is of order 600–700 nm [31,49] and the average grain size is about 120 nm, phonon scattering inside a grain happens infrequently.

### B. Thermal conductivity of individual grains

Once the total phonon lifetime  $\tau_{i,b,\vec{q}} = \Gamma_{i,b,\vec{q}}^{-1}$  has been computed, the thermal conductivity  $\kappa_i$  of grain  $i$  is obtained as a sum over all phonon modes [5,50],

$$\kappa_i(T) = \frac{\hbar}{S_i \delta} \sum_{b,\vec{q}} \nu_{b,\vec{q}}^2 \tau_{i,b,\vec{q}} \omega_{b,\vec{q}} \frac{dN_{b,\vec{q}}^0(T)}{dT}, \quad (11)$$

where  $\delta = 0.335$  nm is the thickness of the graphene monolayer [15],  $S_i$  is the surface area of grain  $i$ , and  $\nu_{b,\vec{q}}$  and  $\omega_{b,\vec{q}}$  are the phonon group velocity and vibrational frequency calculated from the full phonon dispersion based on the nearest-neighbor force constant model [51,52].

### C. Thermal resistor network

In the steady state, the net heat flux through the boundary of each grain must be zero. Therefore, fluxes in and out of its neighbors and any external heating source  $Q_i$  applied to  $i$ th grain must add to zero. This assertion allows us to calculate

the temperature  $T_i$  inside the  $i$ th grain from

$$\sum_{j=\text{n.n.}} G_{ij}(T_i - T_j) + S_i Q_i = 0, \quad (12)$$

with the summation index  $j$  running over all the grains that neighbor grain  $i$ . The thermal conductance  $G_{ij}$  between neighboring grains  $i$  and  $j$  is given by the usual expression

$$G_{ij} = \frac{[d_i \kappa_i(T_i) + d_j \kappa_j(T_j)] A_{ij}}{d_{ij}^2}. \quad (13)$$

Here  $d_{ij} = d_i + d_j$  is the distance between the centers of the two grains, i.e., the length of the straight line connecting the two centers, while  $d_i$  and  $d_j$  are the lengths of the line's segments inside the  $i$ th and  $j$ th grains, respectively.  $A_{ij}$  is the area of the grain contact region given by the product of the length of the grain boundary  $l_{ij}$  separating the two grains and the thickness of the graphene sheet  $A_{ij} = l_{ij} \delta$ . This way we effectively obtain a thermal resistor network, which can be solved iteratively, repeatedly updating the temperature of each grain based on the past values of the temperatures of its neighbors until convergence [53]. We stress that the effect of the grain boundary roughness scattering on heat transport is captured within the thermal conductivity of each grain. We assume there is no interface thermal resistance, because all grains are of the same material and have the same acoustic impedances. We do not account for interface resistance that might stem from grain misorientation.

## IV. RESULTS

We consider a polycrystalline graphene sample of dimensions  $10 \mu\text{m} \times 10 \mu\text{m}$ . The graphene layer consists of 5000 grains, which were generated according to an experimentally relevant distribution (Fig. 2), with the average diameter of about 120 nm. The rms roughness of each grain boundary is assumed to be  $\Delta = 1$  nm.

The thermal transport geometry we consider is similar to the Corbino membrane from Ref. [27]. We assume that graphene is placed on a substrate that has a circular opening of radius  $4 \mu\text{m}$ . The coordinate origin in the simulation domain is the point on the graphene sheet right above the center of the circular opening;  $r$  is the in-plane radial coordinate. The substrate acts as a heat sink and is kept at 300 K, thereby our boundary condition on temperature is  $T(r \geq 4 \mu\text{m}) = 300$  K. We apply a heat source  $Q$  to the grains inside a radius  $r_1 = 1 \mu\text{m}$  around the center and allow heat to diffuse.  $Q$  is determined, upon iteration of the temperature, to ensure the peak temperature in the center to be 20 K above the temperature of the heat sink. Convergence is reached when the total flux entering each grain equals the flux leaving it and the temperatures of all grains reach a constant value. Figure 3 shows a steady-state temperature profile.

Once the temperatures reach a steady state, we extract the effective thermal conductivity in a manner analogous to the experimental setup using the radial heat flow method. We calculate the temperature profile  $T_1$  at all points along an inner ring of radius  $r_1 = 1 \mu\text{m}$  and  $T_2$  along an outer ring of radius  $r_2 = 3 \mu\text{m}$  to obtain an effective thermal conductivity as  $\kappa_{\text{eff}} = \frac{Q \log(r_2/r_1)}{2\pi(T_1 - T_2)}$ . Now, if the sample were uniform and the

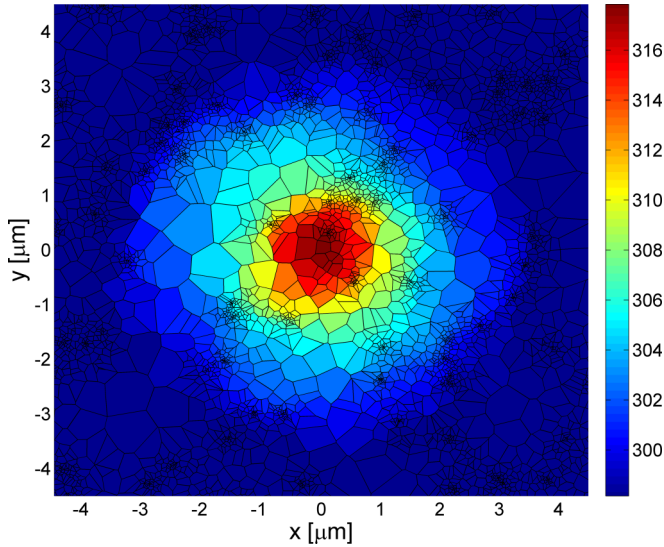


FIG. 3. (Color online) Steady-state temperature profile, represented by color (red is high, blue is low; color bar is in degrees Kelvin) in the  $10 \mu\text{m} \times 10 \mu\text{m}$  polycrystalline graphene sample. Black lines show the grain boundaries. Temperature is resolved at the level of individual grains.

heat flow radial, picking any two points on the circles with radii  $r_1$  and  $r_2$  would yield the same effective thermal conductivity. But, in a polycrystalline sample there will be anisotropy, so it is interesting to see how  $\kappa_{\text{eff}}$  depends on the direction of heat flow: We pick points from the  $r_1$  and  $r_2$  circles at a given angle  $\Theta$  with respect to the  $x$  axis and evaluate  $\kappa_{\text{eff}}$ .

The computed values of  $\kappa_{\text{eff}}$  at room temperature, presented in Fig. 4, show a very strong directional anisotropy, with values ranging from  $350 \text{ W m}^{-1} \text{ K}^{-1}$  in some directions all the way up to  $1500 \text{ W m}^{-1} \text{ K}^{-1}$  in others. The average over all directions, which is the value for which it makes sense to make comparisons to experimental results, is  $600 \text{ W m}^{-1} \text{ K}^{-1}$ , in agreement with the results from Refs. [26,27]. However, the computed values are very sensitive to the amount of grain boundary roughness  $\Delta$ , assumed here to be 1 nm, and the relative topology of the grains. The results presented in Fig. 4 represent only one of an infinite number of different arrangements of grains with varying positions and connections resulting from different possible ways to tessellate the graphene sheet. Even when we fix the size distribution to reproduce the experimental results, as we have done in this study, the number of different arrangements of grains having that size distribution is staggering. Nonetheless, for a given size distribution, all the possible variations will be bounded between two extremes: A series average of thermal conductivity over the grains will produce a lower bound dominated mainly by the many small grains, while a parallel average without the self-consistent iteration of heat flux will provide an upper bound dominated by the large heat flux of the small number of large grains in the tail of the size distribution.

In Fig. 5 we compare the thermal conductivity calculated for the grain distribution depicted in Fig. 3 and over a range of temperatures with the experimental data taken from Cai *et al.* [21]. The two sets of experimental data, depicted in triangles and circles, were obtained from micro-Raman

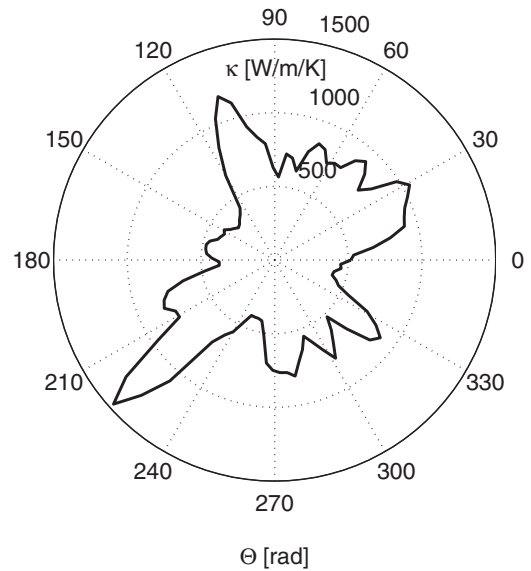


FIG. 4. Polar plot of the directional dependence of thermal conductivity in large-area polycrystalline graphene, showing large anisotropy due to the variation in the relative positions and sizes of grains. The polar angle  $\Theta$  denotes the direction of heat propagation with respect to the  $x$  axis from Figs. 3 and 6, while the radial coordinate corresponds to the magnitude of thermal conductivity (concentric circles with radii in  $500 \text{ W/m K}$  increments are shown).

spectroscopy and correspond to two different objectives used to focus the laser [21]. In the calculations we assume  $\Delta = 0.5 \text{ nm}$  because this value produced better agreement with the

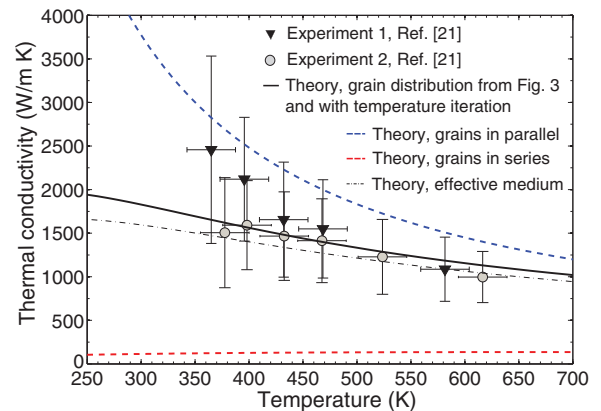


FIG. 5. (Color online) Comparison of the calculated thermal conductivities (curves) with experimental data for suspended CVD graphene taken from Ref. [21] (symbols). The two sets of experimental data (triangles and circles) were obtained from micro-Raman spectroscopy using two different objectives to focus the laser. The black solid curve corresponds to the grain size distribution depicted in Fig. 3 and  $\kappa_{\text{eff}}$  was obtained upon the temperature iteration described in Sec. III C. For the same collection of grains, the upper limit to thermal conductivity would be obtained by connecting them in parallel (dashed blue line). The lower limit corresponds to the same collection of grains in series (dashed red line). Results from the effective medium theory (a single grain having the same average diameter) are presented by the black dash-dot curve.

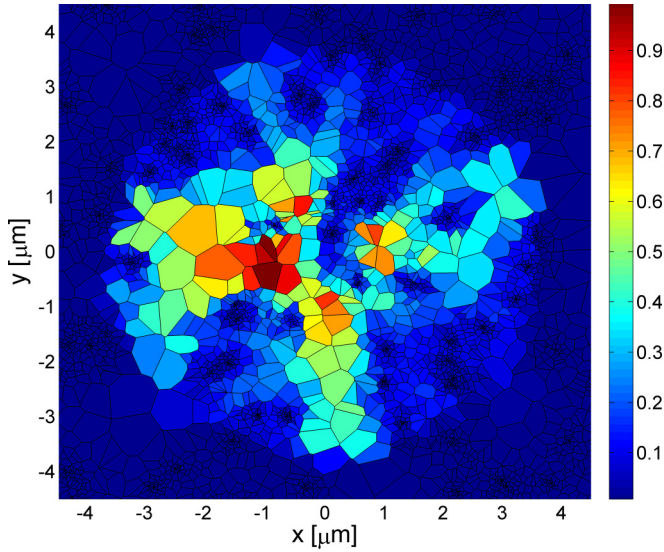


FIG. 6. (Color online) Spatial profile of the normalized heat flux magnitude, represented by color (red is high, blue is low). The grain distribution is the same as in Fig. 3.

experimental data. The black solid curve represents the data obtained after the temperature iteration procedure described in Sec. III C; note that curve passes through all the error bars on the measured data. For the same collection of grains, we present the thermal conductivity that corresponds to all the grains connected thermally in series, based on thermal conductivities of grains alone (dashed red curve); this type of connection puts a lower bound on the conductivity for a given set of grains. Also, we present the thermal conductivity data for all grains connected in parallel (blue dashed curve), which puts an upper bound on the conductivity. Note that the experimental data (with error bars) is below our calculated in-parallel curve, which is an indication that our grain size distribution is realistic. Moreover, differently connected grains would result in quantitatively different thermal conductivity; however, considering the large experimental error bars, a number of grain distributions would likely give reasonable fits, quantitatively slightly different but qualitatively the same as the black curve, which corresponds to one specific distribution. For reference we also show the results from the effective medium theory, calculated with a single grain of the same average diameter as our grain size distribution and plotted in a dash-dot black curve in Fig. 5.

The importance of grain connectivity can be illustrated via the strong directional anisotropy of the normalized heat flux magnitude, shown in Fig. 6.  $\tilde{H}_i$ , the normalized heat flux magnitude of grain  $i$ , is defined here as the sum of the absolute values of all the fluxes entering or leaving each grain through its boundaries with other grains,  $H_i = \sum_j G_{ij}|T_i - T_j|$ , divided

by the largest value  $\max_i\{H_i\}$ . Larger grains typically carry larger heat flux due to the size-dependent thermal conductivity. It is also evident that size alone does not determine the relative contribution to heat conduction. When larger grains neighbor each other and are interconnected, they exchange more heat, thus leading to a form of filamentation: Chains of larger grains contribute to stronger thermal transport, while those grains that are surrounded by smaller ones contribute comparatively less to the overall thermal transport, as evidenced by the smaller normalized heat flux through them. We conclude that both structural morphology and grain connectivity have a strong effect on thermal transport, analogous to their impact on electronic transport in polycrystalline graphene [54].

## V. CONCLUSION

We studied thermal transport in large-area ( $10\ \mu\text{m} \times 10\ \mu\text{m}$ ) polycrystalline graphene samples, such as those commonly grown by CVD on Cu. We developed a model for the grain structure of CVD graphene based on a 2D Voronoi tessellation. To analyze thermal transport in polycrystalline graphene, we solved the phonon Boltzmann transport equation for phonons in a single grain with a generally rough grain boundary, used that result to compute the thermal conductivity in each grain, and lastly iterated the temperature distribution over the large-scale sample based on the heat flux continuity equation for each grain in order to obtain a steady-state temperature profile. Based on our results, we conclude that thermal transport in polycrystalline graphene samples is highly anisotropic and depends strongly on both the individual properties of the grains, i.e., their size and boundary roughness, as well as on their relative positions and interconnections.

Controlling disorder in the form of roughness and grain size distribution is an effective way to tailor the thermal properties of CVD graphene. We envision further customization of heat flow in CVD graphene by controlling the growth of individual grains, which has been experimentally demonstrated [36], and patterning the samples in order to block or conduct heat in particular directions. This effect can be achieved either by controlling the distribution and positions of the areas containing small, few-nanometer-sized grains which efficiently block the flow of heat, or by taking this approach to the extreme and patterning holes in the sample along those directions in which we wish to block the flow of heat. Doing so would produce thermal conduits and allow for a form of thermal interconnects which, combined with graphene-based thermal rectifiers [55,56], form the building blocks of thermal circuits.

## ACKNOWLEDGMENT

This work has been supported by the NSF, awards No. 1122690 (Z.A.) and No. 1201311 (I.K.).

[1] A. A. Balandin, S. Ghosh, W. Bao, I. Calizo, D. Teweldebrhan, F. Miao, and C. N. Lau, *Nano Lett.* **8**, 902 (2008).

[2] S. Ghosh, I. Calizo, D. Teweldebrhan, E. P. Pokatilov, D. L. Nika, A. A. Balandin, W. Bao, F. Miao, and C. N. Lau, *Appl. Phys. Lett.* **92**, 151911 (2008).

- [3] P. Klemens and D. Pedraza, *Carbon* **32**, 735 (1994).
- [4] B. D. Kong, S. Paul, M. B. Nardelli, and K. W. Kim, *Phys. Rev. B* **80**, 033406 (2009).
- [5] D. L. Nika, E. P. Pokatilov, A. S. Askerov, and A. A. Balandin, *Phys. Rev. B* **79**, 155413 (2009); D. L. Nika, S. Ghosh, E. P. Pokatilov, and A. A. Balandin, *Appl. Phys. Lett.* **94**, 203103 (2009).
- [6] J. Lan, J.-S. Wang, C. K. Gan, and S. K. Chin, *Phys. Rev. B* **79**, 115401 (2009).
- [7] A. V. Savin, Y. S. Kivshar, and B. Hu, *Phys. Rev. B* **82**, 195422 (2010).
- [8] W. J. Evans, L. Hu, and P. Keblinski, *Appl. Phys. Lett.* **96**, 203112 (2010).
- [9] E. Munoz, J. Lu, and B. I. Yakobson, *Nano Lett.* **10**, 1652 (2010).
- [10] A. A. Balandin, *Nat. Mater.* **10**, 569 (2011).
- [11] J. H. Seol, I. Jo, A. L. Moore, L. Lindsay, Z. H. Aitken, M. T. Pettes, X. Li, Z. Yao, R. Huang, D. Broido, N. Mingo, R. S. Ruoff, and L. Shi, *Science* **328**, 213 (2010).
- [12] K. Saito, J. Nakamura, and A. Natori, *Phys. Rev. B* **76**, 115409 (2007).
- [13] Y. Xu, X. Chen, B.-L. Gu, and W. Duan, *Appl. Phys. Lett.* **95**, 233116 (2009).
- [14] J.-W. Jiang, J.-S. Wang, and B. Li, *Phys. Rev. B* **79**, 205418 (2009).
- [15] Z. Aksamija and I. Knezevic, *Appl. Phys. Lett.* **98**, 141919 (2011).
- [16] S. Bae, H. Kim, Y. Lee, X. Xu, J.-S. Park, Y. Zheng, J. Balakrishnan, T. Lei, H. Ri Kim, Y. I. Song, Y.-J. Kim, K. S. Kim, B. Ozyilmaz, J.-H. Ahn, B. H. Hong, and S. Iijima, *Nat. Nano.* **5**, 574 (2010).
- [17] X. Li, W. Cai, J. An, S. Kim, J. Nah, D. Yang, R. Piner, A. Velamakanni, I. Jung, E. Tutuc, S. K. Banerjee, L. Colombo, and R. S. Ruoff, *Science* **324**, 1312 (2009).
- [18] P. Y. Huang, C. S. Ruiz-Vargas, A. M. van der Zande, W. S. Whitney, M. P. Levendorf, J. W. Kevek, S. Garg, J. S. Alden, C. J. Hustedt, Y. Zhu, J. Park, P. L. McEuen, and D. A. Muller, *Nature (London)* **469**, 389 (2011).
- [19] K. Kim, Z. Lee, W. Regan, C. Kisielowski, M. F. Crommie, and A. Zettl, *ACS Nano* **5**, 2142 (2011).
- [20] P. Nemes-Incze, K. J. Yoo, L. Tapasztó, G. Dobrik, J. Lábár, Z. E. Horvth, C. Hwang, and L. P. Biró, *Appl. Phys. Lett.* **99**, 023104 (2011).
- [21] W. Cai, A. L. Moore, Y. Zhu, X. Li, S. Chen, L. Shi, and R. S. Ruoff, *Nano Lett.* **10**, 1645 (2010).
- [22] S. Chen, A. L. Moore, W. Cai, J. W. Suk, J. An, C. Mishra, C. Amos, C. W. Magnuson, J. Kang, L. Shi, and R. S. Ruoff, *ACS Nano* **5**, 321 (2011).
- [23] D. L. Nika and A. A. Balandin, *J. Phys.: Condens. Matter* **24**, 233203 (2012).
- [24] A. Glatz and I. S. Beloborodov, *Phys. Rev. B* **80**, 245440 (2009).
- [25] I. S. Beloborodov, A. V. Lopatin, F. W. J. Hekking, R. Fazio, and V. M. Vinokur, *Europhys. Lett.* **69**, 435 (2005).
- [26] I. Vlassiouk, S. Smirnov, I. Ivanov, P. F. Fulvio, S. Dai, H. Meyer, M. Chi, D. Hensley, P. Datskos, and N. V. Lavrik, *Nanotechnology* **22**, 275716 (2011).
- [27] C. Faugeras, B. Faugeras, M. Orlita, M. Potemski, R. R. Nair, and A. K. Geim, *ACS Nano* **4**, 1889 (2010).
- [28] A. Bagri, S.-P. Kim, R. S. Ruoff, and V. B. Shenoy, *Nano Lett.* **11**, 3917 (2011).
- [29] Y. Lu and J. Guo, *Appl. Phys. Lett.* **101**, 043112 (2012).
- [30] A. Y. Serov, Z.-Y. Ong, and E. Pop, *Appl. Phys. Lett.* **102**, 033104 (2013).
- [31] Z. Aksamija and I. Knezevic, *Phys. Rev. B* **86**, 165426 (2012).
- [32] M.-H. Bae, Z. Li, Z. Aksamija, P. N. Martin, F. Xiong, Z.-Y. Ong, I. Knezevic, and E. Pop, *Nat. Commun.* **4**, 1734 (2013).
- [33] J. C. Koepke, J. D. Wood, D. Estrada, Z.-Y. Ong, K. T. He, E. Pop, and J. W. Lyding, *ACS Nano* **7**, 75 (2013).
- [34] Z. Aksamija and I. Knezevic, *Phys. Rev. B* **88**, 155318 (2013).
- [35] M. Maldovan, *J. Appl. Phys.* **110**, 114310 (2011).
- [36] Q. Yu, L. A. Jauregui, W. Wu, R. Colby, J. Tian, Z. Su, H. Cao, Z. Liu, D. Pandey, D. Wei, T. F. Chung, P. Peng, N. P. Guisinger, E. A. Stach, J. Bao, S.-S. Pei, and Y. P. Chen, *Nat. Mater.* **10**, 443 (2011).
- [37] M. Bartkowiak and G. D. Mahan, *Phys. Rev. B* **51**, 10825 (1995).
- [38] J.-P. Crocombette and L. Gelebart, *J. Appl. Phys.* **106**, 083520 (2009).
- [39] J.-S. Ferenc and Z. Nda, *Physica A* **385**, 518 (2007).
- [40] A. Priolo, H. M. Jaeger, A. J. Dammers, and S. Radelaar, *Phys. Rev. B* **46**, 14889 (1992).
- [41] Z. Fan, Y. Wu, X. Zhao, and Y. Lu, *Comp. Mater. Sci.* **29**, 301 (2004).
- [42] D. Singh, J. Y. Murthy, and T. S. Fisher, *J. Appl. Phys.* **110**, 113510 (2011).
- [43] L. Lindsay, D. A. Broido, and N. Mingo, *Phys. Rev. B* **82**, 115427 (2010).
- [44] P. Carruthers, *Rev. Mod. Phys.* **33**, 92 (1961).
- [45] J. E. Graebner, M. E. Reiss, L. Seibles, T. M. Hartnett, R. P. Miller, and C. J. Robinson, *Phys. Rev. B* **50**, 3702 (1994).
- [46] Z. Wang and N. Mingo, *Appl. Phys. Lett.* **99**, 101903 (2011).
- [47] V. Adamyan and V. Zavalniuk, *J. Phys.: Condens. Matter* **24**, 415401 (2012).
- [48] J. Ziman, *Electrons and Phonons: The Theory of Transport Phenomena in Solids* (Oxford University Press, Oxford, 1960).
- [49] Z. Aksamija and I. Knezevic, *Phys. Rev. B* **82**, 045319 (2010).
- [50] S. Ghosh, D. L. Nika, E. P. Pokatilov, and A. A. Balandin, *New J. Phys.* **11**, 095012 (2009).
- [51] R. Saito, G. Dresselhaus, and M. S. Dresselhaus, *Physical Properties of Carbon Nanotubes* (Imperial College Press, London, 1998).
- [52] J. Zimmermann, P. Pavone, and G. Cuniberti, *Phys. Rev. B* **78**, 045410 (2008).
- [53] L. Braginsky, N. Lukzen, V. Shklover, and H. Hofmann, *Phys. Rev. B* **66**, 134203 (2002).
- [54] A. W. Tsen, L. Brown, M. P. Levendorf, F. Ghahari, P. Y. Huang, R. W. Havener, C. S. Ruiz-Vargas, D. A. Muller, P. Kim, and J. Park, *Science* **336**, 1143 (2012).
- [55] N. Yang, G. Zhang, and B. Li, *Appl. Phys. Lett.* **95**, 033107 (2009).
- [56] W.-R. Zhong, W.-H. Huang, X.-R. Deng, and B.-Q. Ai, *Appl. Phys. Lett.* **99**, 193104 (2011).